

# Chandra X-ray Observation of a Mature Cloud-Shock Interaction in the Bright Eastern Knot Region of Puppis A

Una Hwang<sup>1,2</sup>, Kathryn A. Flanagan<sup>3</sup>, Robert Petre<sup>1</sup>

## ABSTRACT

We present Chandra X-ray images and spectra of the most prominent cloud-shock interaction region in the Puppis A supernova remnant. The Bright Eastern Knot (BEK) has two main morphological components: (1) a bright compact knot that lies directly behind the apex of an indentation in the eastern X-ray boundary and (2) lying 1' westward behind the shock, a curved vertical structure (bar) that is separated from a smaller bright cloud (cap) by faint diffuse emission. Based on hardness images and spectra, we identify the bar and cap as a single shocked interstellar cloud. Its morphology strongly resembles the “voided sphere” structures seen at late times in Klein et al.’s experimental simulations of cloud-shock interactions, when the crushing of the cloud by shear instabilities is well underway. We infer an interaction time of roughly 3 cloud-crushing timescales, which translates to 2000-4000 years, based on the X-ray temperature, physical size, and estimated expansion of the shocked cloud. This is the first X-ray identified example of a cloud-shock interaction in this advanced phase. Closer to the shock front, the X-ray emission of the compact knot in the eastern part of the BEK region implies a recent interaction with relatively denser gas, some of which lies in front of the remnant. The complex spatial relationship of the X-ray emission of the compact knot to optical [O III] emission suggests that there are multiple cloud interactions occurring along the line of sight.

*Subject headings:* instabilities; ISM:clouds; ISM: supernova remnants; X-rays: individual (Puppis A)

---

<sup>1</sup>NASA Goddard Space Flight Center, Code 662, Greenbelt MD 20771; hwang@milkyway.gsfc.nasa.gov

<sup>2</sup>Department of Physics and Astronomy, The Johns Hopkins University, 3400 Charles St, Baltimore MD 21218

<sup>3</sup>Kavli Institute for Astrophysics and Space Research, MIT, 77 Massachusetts Ave, Cambridge MA 02139

## 1. Introduction

Puppis A is a middle-aged member of the class of oxygen-rich remnants that includes Cassiopeia A. The optical emission from these remnants is dominated by oxygen, requiring massive progenitors that synthesized the oxygen during their hydrostatic evolution. Puppis A has faint oxygen-dominated filaments (Winkler & Kirshner 1985), whose proper motions and positions give a dynamical age of  $3700 \pm 300$  yr for the remnant (Winkler et al. 1988). Oxygen ejecta also leave their imprint on the X-ray line emission in high spectral resolution data from the Einstein Observatory; the implied presence of at least  $3 M_{\odot}$  of O and Ne ejecta requires a progenitor with an initial mass exceeding  $25 M_{\odot}$  (Canizares & Winkler 1981). A massive progenitor for Puppis A is confirmed by the discovery of an isolated X-ray emitting neutron star associated with the remnant (Petre et al. 1996), with no confirmed period (Pavlov et al. 1999, 2002) and no radio counterpart (Gaensler et al. 2000).

Based on the properties of the fast O-rich, and slower N-rich, optical knots, Chevalier (2005) concludes that the progenitor of Puppis A underwent substantial mass loss before exploding as a SN IIL/b. The red supergiant wind was likely to have been clumpy, and is expected to have reached about 7 pc from the explosion center, in comparison to the full 32 pc extent of Puppis A. This is consistent with the presence of optically identified N-rich wind material in the interior of the remnant, and indicates that the majority of the material with which the remnant has interacted is interstellar rather than circumstellar. Earlier in the remnant’s evolution, the clumpiness of the circumstellar environment may have also aided in the formation of ejecta bullets by Rayleigh-Taylor instabilities (Jun et al. 1996).

Since massive stars typically evolve in associations and modify their surroundings through their stellar winds, it is not surprising that Puppis A sits in an exceptionally complex interstellar environment. Indeed, its X-ray properties are now largely shaped by its interaction with its surroundings. The remnant shows increasing X-ray surface brightness west to east that reflects a large-scale increase in the ambient density of roughly a factor of four (Petre et al. 1982).

The brightest X-ray feature is dubbed the Bright Eastern Knot (BEK) for its location at the eastern edge of the shock front, and is understood to arise from interaction of the shock wave with an interstellar cloud. The BEK also dominates the remnant at radio wavelengths (Dubner et al. 1991), and its high radio brightness is consistent with the cloud-shock interaction scenario. The high magnetic fields needed for particle acceleration to produce the radio emission can be generated in vortices that are formed as a cloud is disrupted by the shock (Stone & Norman 1992). In the northern interior of the remnant, the Northern Knot (NK) is a more isolated example of a shocked interstellar cloud.

The presence of an extremely massive and extensive atomic/molecular cloud along the linear northeastern edge of Puppis A (in the direction towards the Galactic Plane), is established by observations of HI and CO emission (Dubner & Arnal 1988, Reynoso et al. 1995). Infrared observations further reveal that the tip of the eastern molecular cloud is probably projected in front of the remnant’s eastern border (Arendt et al. 1990). Other massive HI and CO clouds to the southeast and north are also likely to be interacting with the remnant (Reynoso et al. 1995). Indeed, the entire remnant sits at the periphery of a very large HI shell of roughly 120 pc diameter and 30,000  $M_{\odot}$  estimated mass (Dubner & Arnal 1988). In this context, the Bright Eastern Knot is just one part of an extremely complex and extensive interstellar environment.

In this paper, we present Chandra images and spectra of the most prominent shocked cloud interaction region in Puppis A—the Bright Eastern Knot. Cloud-shock interactions have been studied most extensively in X-ray and optical studies of the Cygnus Loop (Levenson et al. 2002, 2005, Leahy 2004, Patnaude et al. 2002, Graham et al. 1995, Fesen et al. 1992). The Cygnus Loop is expanding into a cavity wall, which is itself a large expanding cloud (Leahy 2003). The references above identify a number of cloud-shock interactions in various parts of the remnant, most of which are relatively recent. They are manifested by soft emission produced behind the decelerated shock propagating into the cloud and enhanced harder X-ray emission produced behind shocks reflected back into already-shocked gas. The current location of the blast wave in the intercloud gas is established by the nonradiative optical emission. It will be seen that our study of Puppis A is complementary to those of the Cygnus Loop in two ways: the  $\sim 700$  km/s intercloud shock velocities are higher than the 300-400 km/s velocities typical of the Cygnus Loop, and at least one identified cloud-shock interaction in Puppis A is significantly more mature than those seen so far in the Cygnus Loop.

## 2. Chandra Images and Spectra

### 2.1. X-ray Color Images

We observed the Bright Eastern Knot in Puppis A using the Chandra Observatory’s Advanced CCD Imaging Spectrometer (ACIS) for 10.6 ks, using only the backside-illuminated S3 chip to avoid telemetry saturation in the event of strong background flares. The mirrors provide images with  $0.5''$  angular resolution over the  $8' \times 8'$  single-chip field of view. The CCD was operated in Graded mode, wherein the CCD events are characterized onboard the spacecraft to reduce the telemetry load; the events thus could not be corrected for charge transfer inefficiency. The count rate was relatively stable throughout the observation.

We supplement the Chandra images with lower resolution, but larger field of view images from XMM-Newton and ROSAT. We use the XMM-Newton EPIC PN image from a 9.7 ks exposure, which provides a view of the  $\sim 30'$  region near the BEK with a  $6''$  FWHM point-source image core. The XMM-Newton EPIC CCDs provide similar spectral resolution as the Chandra ACIS instruments<sup>1</sup>. The ROSAT PSPC imaged the entire remnant in three pointings of 2.3 to 7.9 ks exposure with  $25''$  FWHM angular resolution and limited spectral resolution over its 0.2-2 keV bandwidth. We reduced the PSPC data using the algorithms and software described in Snowden et al. (1994) to model and subtract the background. The EPIC and PSPC data are used here for spectral imaging only, and not for detailed spectral analysis.

The Chandra observation is shown in a three color rendering in Figure 1 (soft energies 0.4-0.7 keV, covering O emission and continuum, in red; medium energies 0.7-1.2 keV, covering Ne and Fe L, in green; hard energies  $>1.2$  keV, in blue). Intricate filamentary structure is evident in the image field. The indentation seen in the eastern X-ray boundary strongly suggests that the shock wave is wrapping around an obstacle of approximately  $40''$  angular extent on the sky (0.4 pc at a distance of 2.2 kpc for Puppis A: Reynoso et al. 2003, 1995, Winkler et al. 1988, Dubner & Arnal 1988; though Woermann et al. 2000 suggest a smaller distance). A compact, X-ray bright region is located immediately west of this indentation. Roughly  $1'$  further west lies a more extended vertical structure (henceforth the bar) that bends sharply inward at its bright southern end, has a sharp boundary to the east and a more diffuse boundary to the west. The bar is separated by lower surface-brightness emission from a smaller cloud (cap) lying  $4'$  away near the western edge of the Chandra field. The bar appears to separate the relatively soft spectra found to the east from harder spectra to the west.

The EPIC PN spectral images shown in Figure 2 use the same energy cuts as the Chandra ACIS spectral images, whereas the ROSAT PSPC mosaics of the entire remnant use the three standard PSPC energy bands (Snowden et al. 1994; soft bands 1L and 2 covering energies 0.11-0.28 keV in red, medium bands 4 and 5 covering 0.44-1.21 keV in green, and hard bands 6 and 7 covering 0.73-2.04 keV in blue). These images verify that the bar and cap behind the shock front indentation are spectrally similar. They also show that a large region to the south of the BEK is spectrally soft, whereas the regions to the north of the BEK and running behind the entire straight northeastern shock front are spectrally hard. This large-scale band of hard emission has been previously noted from ROSAT All-Sky

---

<sup>1</sup>The EPIC MOS camera data are not useful for studying the region around the BEK because they were collected with the central chip in partial window mode in order to avoid pulse pile-up. The high count rates also cause strong telemetry dropout that is evident in the light curves from all the EPIC detectors.

Survey and ASCA observations (Aschenbach 1994, Tamura 1995). Just south of this hard region, relatively faint emission from the nearby Vela supernova remnant is seen extending beyond Puppis A to the east and southwest in the PSPC mosaic, but is appreciable only in the softest image because of Vela’s extremely soft spectrum (see Lu & Aschenbach 2000). It is likely that this entire Vela filament is projected in front of Puppis A. As in the smaller Chandra images, filamentation is observed throughout the remnant (and is seen to even better advantage in the ROSAT High Resolution Imager mosaic of Petre et al. 1996).

## 2.2. Spectral Maps

Since spectral hardness may be affected not only by temperature, but also by column density, relative element abundances, and the ionization state of the X-ray emitting gas, we examined the X-ray spectra across the ACIS field. The source region on the CCD was divided into a grid of continuous regions for spectral analysis, starting with a basic box-shaped region that was further subdivided according to the number of counts contained. The 250 spectral regions range from 12.5'' to 50'' boxes or rectangles. Spectra typically contained 7000-12000 counts, though the actual number of counts ranged from 4000 to 16000. Although we do not use the EPIC data for spectral analysis here—there are differences in point-spread function that would make a detailed comparison with the Chandra data difficult—we have verified that the general *qualitative* features of the ACIS spectral results are also seen in the EPIC data.

To fit the spectra, we used simple models that account for the nonequilibrium ionization (NEI) state of the gas, where the ionization state is characterized by an ionization timescale or “age”, defined as the product  $n_e t$  of electron density  $n_e$  and time  $t$  since shock-heating of the gas. Specifically we use the *pshock* model in XSPEC, which assumes a single temperature and a range of ionization ages, which we take from zero up to a fitted maximum value. This should better describe the complex spectra in extended spatial regions than would a single-temperature, single-ionization age NEI model, and we generally find that to be the case for these data. Solar abundances from Anders & Grevesse (1989) are used throughout. To model the buildup of contaminants on the detector surface, we include the ACISABS model in our spectral fits, specifying the number of days since launch for the observation (833). To subtract the background, we use local off-source regions.

Figure 3 shows the spectral grid regions and image maps for the fitted temperatures, ionization ages, and column densities. The BEK region shows significant spectral complexity, with low temperatures kT of  $\sim 0.3$  keV near the eastern indentation, to 0.5-0.6 keV in the regions that cover the bar and cap, all the way up to high temperatures above 0.8 keV in

some low surface brightness regions. For the four representative regions indicated in Figure 3, the spectra and fitted models are shown in Figure 4, and the fitted parameters given in the Table. The errors cited in the Table and discussed in the paper are the 90% confidence ranges for a single interesting parameter, corresponding to  $\Delta\chi^2=2.71$ .

There are two important features to note in the spectral parameter maps of the BEK. First, spectra in the bar and cap (as well as most of the associated lower surface brightness regions) are seen to be characterized by similar temperature, maximum ionization age, and column density. Second, the regions to the east and far southeast (i.e., the lower left region of the ACIS field) of the bar are spectrally very distinct: their temperatures are lower (at  $\sim 0.3$  keV compared to  $\sim 0.6$  keV for the bar and cap), ionization ages lower (below  $10^{11}$  cm $^{-3}$ s compared to several  $10^{11}$  cm $^{-3}$  s), and column densities higher ( $3\text{-}5 \times 10^{21}$  cm $^{-2}$  compared to  $1\text{-}2 \times 10^{21}$  cm $^{-2}$ ).

A closer look at the temperature change from the compact knot to the bar is given in Figure 5. The spectra in a series of adjacent rectangular regions were fitted with single-temperature parallel shock models assuming solar abundances to obtain the temperature, ionization age, and column density. The temperature change across the series is gradual and smooth across the first four regions, rather than being abrupt, but the changes are more abrupt for the other parameters: the column density drops sharply for the fourth region, just as the ionization age jumps up.

For spectra with at least 6000-7000 counts, typical errors are a few to 10% for the fitted temperature, and roughly 20% for the column density and ionization age. In the cases where the spectra contain fewer counts, these errors are correspondingly larger, up to 50-60% or higher for the column density and ionization age. The temperature, however, is determined to 10% or better in nearly all cases. For most of the spectra, there is a clear-cut global minimum, but in a number of more ambiguous cases, there are two comparable local minima—usually one with very low column density and high temperature, and the other with high column density and low temperature. This accounts for a few isolated cool (or hot) regions in the temperature map in Figure 3. The column densities fitted for some regions are unrealistically low for Puppis A ( $< 10^{20}$  cm $^{-2}$ ), and most likely indicate that the simplified model assumptions imposed for the spectral fits are inadequate.

We take  $\chi_r^2 = \chi^2/\nu$  as the goodness-of-fit criterion, where  $\nu$  is the number of degrees of freedom. These values are shown in Figure 6. In general, they are less than 2, which we loosely take to be a reasonably acceptable fit in view of the limitations of the spectral model and systematic effects in the data. Some 30% of the spectra fitted have  $\chi^2/\nu$  greater than 2, however, and as these are not necessarily the spectra with the highest signal-to-noise, the poorness of fit must be in part due to the shortcomings of the spectral model. We tried a

few more complex models to try to improve these fits, and found the largest improvements came from allowing the overall O-Ne element abundances to be fitted independently from the others (while tied in their solar abundance ratio). An abundance enhancement for these two elements of 2-3 times their solar value greatly improves the fits in a subset of the spectra that initially had poor fits. An example is given in the table (region 214). Where the improvement in  $\chi^2$  is statistically significant (we took a  $\Delta\chi^2/\chi_r^2$  value of 7.88 as the cutoff), we replaced the original fit with the revised fit, as shown in Figure 6. In the end, roughly one-fifth of all the regions remain relatively poorly fitted with  $\chi^2/\nu > 2$ .

In the revised fits, the abundance enhancements generally occur in localized pockets. For the most part these are outside the bar and cap—to the north, southeast and east (north of the compact knot). field. In about half of the cases where the enhancements occur, the fitted temperature does change, usually from  $\sim 0.6$  keV down to a lower value, with relatively high ionization ages that are well above  $10^{11}$  cm $^{-3}$ s (note that the cool regions near the compact knot have lower ionization ages below  $10^{11}$  cm $^{-3}$ s). In the following section, we will interpret the bar and cap as components of a single, shocked interstellar cloud. As would be expected in this case, the dense cloud material is not as contaminated by ejecta than is less dense intercloud gas. While the shocked cloud is slightly less coherent in the revised temperature map, it remains readily identifiable.

Enhanced element abundances are not generally expected in older remnants, but in Puppis A they are in line with the X-ray results of Canizares & Winkler (1981), the optical identification of ejecta by Winkler & Kirshner (1985), and the expectation that the formation of ejecta clumps was aided by Rayleigh-Taylor instabilities arising from the interaction of the shock with a clumpy circumstellar and interstellar environment. Furthermore, the BEK region is just a few arcminutes beyond the location of a number of optically-emitting O ejecta knots, which are preferentially located toward the east (see Winkler et al. 1988). Abundance enhancements have also been noted in the Cygnus Loop. Those found in the center of the Cygnus Loop remnant have been interpreted as being due to enrichment by ejecta (Miyata et al. 1998), whereas the enhancements in the southwest have been suggested to be the result of enrichment of the ISM by an earlier supernova explosion (Leahy 2004).

### 3. Discussion

#### 3.1. Cloud-Shock Interaction

The X-ray images and spectra of the bar and cap in Puppis A suggest that they may be components of a single physical structure. We interpret this composite structure to be

an interstellar cloud that has been shocked, and is in the process of being disrupted by hydrodynamic instabilities.

The basis of our premise is that the morphology of the bar and cap strongly resembles those seen in experimental simulations of the interaction of supernova shock waves with dense interstellar clouds by Klein et al. (2003). Taken together, the bar and cap suggest a spherical shell whose hemispheres have been pulled apart—a “voided sphere”, as described by Klein et al. and pictured in their Figure 15. Though the cloud-shock interaction occurs over hundreds of years on parsec scales in supernova remnants, its morphology and evolution can be simulated in laboratory experiments of some 20 orders of magnitude smaller spatial and temporal scale by virtue of the self-similarity of the hydrodynamics under certain transformations (see Klein et al. 2003 and Ryutov et al. 1999 for details). The experiments involve a dense 100  $\mu\text{m}$  copper ball representing the interstellar cloud embedded in low-density plastic representing the intercloud medium, with a density contrast of roughly a factor of ten. A strong Mach 10 shock wave is initiated in the plastic by laser-produced X-rays that ablate the plastic. The copper sphere is vaporized before arrival of the shock wave by heating from X-rays coming from the gold capsule encasing the system. The progress of the interaction is recorded edge-on by doing the experiment in multiple sets and using an X-ray backlight to make shadowgrams at different time delays relative to the beginning of the laser pulse.

As described by Klein et al., the characteristic time scale of the interaction is the cloud-crushing time  $t_{cc}$ , which is defined as  $a_o/v_s$ , where  $a_o$  is the initial radius of the cloud and  $v_s$  is the velocity of the shock in the cloud. For a density enhancement of  $\chi$  for the cloud relative to the intercloud medium, the velocity of the blast wave in the intercloud medium  $v_b$  is decreased by a factor of  $\chi^{1/2}$  within the cloud, so that  $v_s = v_b/\chi^{1/2}$ . For the Klein et al. experimental configuration, the cloud-crushing time is 8 ns, and the experiment follows the progress of the cloud-shock interaction for several  $t_{cc}$ . For collisionless strong shocks where conduction, radiation, and viscosity may reasonably be ignored,  $t_{cc}$  is the single relevant parameter for describing the evolution of the system.

The experimental results are documented in detail in Figures 14 and 15 of Klein et al. As the shock traverses the cloud, the cloud is initially compressed along the direction of the shock velocity, then begins to expand in the orthogonal direction because the shocks are weaker at the sides than along the front and back of the cloud. The cloud takes on an umbrella-like shape as arms begin to form at the sides of the cloud from the action of shear instabilities. As the cloud expands into the intercloud medium, and hydrodynamical shear flow instabilities take their toll, the front and back faces of the cloud begin to separate from each other at a time of roughly 3  $t_{cc}$  (see the  $t=43.6$  ns radiogram in Klein et al.). This is the “voided sphere” morphology that is displayed by the bar and cap structure in Puppis A. We believe

this is the first instance in which such a structure has been identified astrophysically. The cloud-shock interactions studied in the Cygnus Loop (see references cited in the introduction) are all in an earlier phase ( $\sim t_{cc}$ ), which is too early for development of the voided sphere morphology.

The voided sphere structure is confirmed in three-dimensional hydrodynamical simulations of the interaction by Klein et al. (their Figure 19), but interestingly, is not manifested in two-dimensional simulations. Evidently, the third dimension is critical to the development of the instability that shapes the cloud at late times. The simulations also show that the face of the cloud closest to the shock front (in our case, this would be the eastern edge of the bar) has an irregular and fluted outer surface, though this is not particularly apparent in either our X-ray images or the experimental radiograms.

To translate the interaction time for the cloud in Puppis A into approximate years, we consider the size and temperature of the cloud. For a distance of 2.2 kpc, the angular size of the cloud, which is about 4' east-west and 4.7' north-south, translates to 2.5 by 3.0 pc. We take the current average “radius” of the cloud to be about 1.4 pc. By visual examination of the experimental radiograms, the size of the cloud at time  $3.7 t_{cc}$  ( $t=43.6$  ns), is about 1.3 times its original axial dimension along the shock velocity and 2.7 times its original dimension in the orthogonal direction. We thus take the average expansion of the cloud at this epoch to be factor of 2, keeping in mind a roughly 30% error, and the possibility that the actual amount of compression might vary depending, for example, on the density enhancement of the cloud. We thus estimate the original cloud radius to be about 0.7 pc, or  $2.2 \times 10^{13}$  km. The temperature of the X-ray emitting gas associated with the cloud is 0.6 keV, which corresponds to a shock velocity of 700 km/s if we assume there is full equipartition of the shock energy between electrons and ions. The cloud crushing time may then be estimated as  $a_o/v_s = 980$  years, give or take some 30%. Taking the epoch of the interaction to be  $3.7 t_{cc}$ , this translates to an interaction age of 2000-4000 years. This is a significant fraction of the estimated remnant age of  $3700 \pm 300$  (Winkler et al. 1988), and even exceeds it at its upper end, so we take the lower end of the interaction age range as being more plausible.

In fact, a 3700 yr age for the remnant may seem low given that it implies rather high average expansion velocities of 5000 km/s for the western limb (for the expansion center determined by Winkler et al. 1988), but this dynamical age should be an upper limit unless the optical knots have somehow been accelerated rather than decelerated. Somewhat lower average expansion velocities of 3000 km/s are determined for the eastern limb, as might be expected given the significant and widespread deceleration of the shock by large molecular and interstellar clouds.

As an order-of-magnitude check on our inferred interaction time, we may use the distance

of the shocked cloud from the optical expansion center determined by Winkler et al. (1988). The ratio of the radial distance from the expansion center to the shocked cloud compared to the radial distance to the farthest region on the western limb is about 0.55. We can estimate that the shock would have reached the location of the cloud in 55% of its 3700 yr age, or 2000 yrs, if we assume for this purpose that there has been minimal deceleration to the western tip of the remnant, and that this cloud is the first major obstacle encountered by the shock in the east. Then the shock time of the cloud was 1700 years ago, which is in relatively good agreement with the lower end of the range of interaction times inferred from the morphology and spectrum of the cloud.

In reality, the initial shock-cloud interaction could actually have occurred somewhat earlier than our estimate. First, we have probably underestimated the shock velocity in the cloud by assuming full equipartition of the ion and electron energy. This is not self-consistent, since only partial equipartition is achieved at the shock velocity of 700 km/s that we have determine for the cloud (Rakowski et al. 2003), and a higher shock velocity would decrease the interaction time. Second, the current location of the cloud is likely to be farther from the (optically determined) expansion center than its original location because the shock interaction accelerates the cloud so that it is eventually co-moving with the shocked intercloud gas (McKee, Cowie & Ostriker 1978, Klein et al. 1994). This acceleration takes place on a timescale of a few  $t_{cc}$ , so that our cloud should by now be moving with the intercloud gas.

The density of the shocked cloud may be obtained from the spectrally fitted ionization age  $n_e t$ , which is the product of electron density and shock time, and the estimated shock-cloud interaction time. The fitted ionization age is the maximum value required in the models, which include a range of ionization ages from zero up to the maximum. From Figure 3, we take the typical maximum ionization age in the shocked cloud region of the BEK to be  $5 \times 10^{11} \text{ cm}^{-3}\text{s}$ . We may then divide out an interaction time of 2000 yr, at the more plausible lower end of the estimated range as discussed above. To relate the electron density in the shocked gas to the initial density of the cloud, we first note that the gas in the shocked cloud is compressed by a factor of 2 over its original density according to Klein et al. (1994). We can then relate the electron density  $n_e$  in the shocked cloud to the initial H density  $n_{H_0}$  in the unshocked cloud as  $n_e = 1.23n_H = 2.46n_{H_0}$  for a solar abundance plasma, to obtain a corresponding initial average H density in the cloud of  $3 \text{ cm}^{-3}$ . An estimated factor of ten enhancement of the density in the cloud (i.e., as in the experimental simulations) implies local interstellar densities of  $0.3 \text{ cm}^{-3}$ . The inferred local interstellar density may be as low as  $0.15 \text{ cm}^{-3}$  if we consider the upper limit of 4000 yr estimated for the interaction age. A  $> 3$  times higher density of  $10 \text{ cm}^{-3}$  is obtained for the BEK region from analysis of the Einstein High-Resolution X-ray images (Petre et al. 1982), but this is for a

higher-surface brightness region centered on the more recently shocked compact knot that lies eastward of the bar and cap. All of these estimates are rather uncertain, but serve to illustrate the possibility of diagnosing shock-cloud interactions from a combination of X-ray observations and laboratory experiments.

### 3.2. Projection Effects in the BEK

The region of the BEK immediately behind the shock front is spectrally distinct: the temperatures are low, ionization ages low, and the column densities higher than elsewhere in the ACIS field. The 0.3 keV temperature determined for this region is supported by the presence of exceptionally bright optical coronal [Fe XIV]  $\lambda$  5303Å emission (Teske & Petre 1987). This emission can arise in relatively hot plasmas with a narrow range of temperatures between  $kT = 0.07$ -0.3 keV that overlaps the X-ray measured temperature at its upper end. In the western region, where the fitted X-ray temperatures are higher, [Fe XIV] emission is not prominent.

The low temperatures in this region suggest slow shocks propagating into relatively dense clouds. A simple scaling of the X-ray emitting temperatures suggests that the density of the compact cloud currently being encountered by the shock is some 4 times higher than that of the older shocked cloud discussed above, though this is obviously a crude estimate that ignores the complications due to multiple shock reflections. A close look at the temperature behavior at the interface between the  $\sim 0.3$  keV emission associated with the compact knot and the hotter gas associated with the bar and cap shows that the temperature changes gradually, presumably due to a combination of projection effects and the deceleration of the shock upon hitting the large eastern molecular cloud with which it is now interacting. The sharp increase in the column density is consistent with the presence of dense foreground gas associated with these clouds, as observed by IRAS (Arendt et al. 1990). The relatively low ionization ages determined for this portion of the BEK, combined with the compact morphology of the knot at the head of the indentation, suggests a relatively recent interaction, consistent with its position at the eastern outer edge of the remnant. The sharp jump in ionization ages is somewhat puzzling. One speculative possibility is that the shock interacted primarily with diffuse intercloud gas for some time after encountering the cloud undergoing the shear instability before being strongly decelerated by the large molecular cloud system with which it is now interacting.

Diffuse and filamentary [O III] emission are also present in this region of the BEK. The [O III] image from Blair et al. (1995) is shown in Figure 7 with the Chandra X-ray image and

contours overlaid.<sup>2</sup> The optical coordinates were registered using HST Guide Stars, but no effort was made to correct for proper motions, which would in any case be slight. As noted by Blair et al., the [O III] emitting filaments have clearly been shocked, with a velocity of 160-180 km/s determined from the UV spectrum of one of the filaments. At these velocities, the shock is clearly propagating into very dense material. A correlation between the optical and X-ray emission is not expected, since the temperatures behind these shocks are too low to produce X-ray emission. It is notable, however, that the [O III] is located significantly beyond the eastern boundary of the X-ray emission, with the northern and southern edges of the indentation in the X-ray emission emerging from within the optical boundaries. The [O III] would thus appear to indicate the easternmost extent of the blast wave in this region, except that the X-ray morphology strongly suggests a shock wrapping around an obstacle. The pronounced indentation of the X-ray emitting shock at the cloud indicates that this obstacle is probably quite extended along the line of sight. The situation here suggests that projection effects are important, with multiple clouds in the line of sight—a possibility previously noted by Blair et al. (1995). It is certainly plausible that the dense molecular gas with which the remnant is now interacting would be associated with clouds with a spectrum of sizes and masses. Petre et al. (1982), for example, estimate density inhomogeneities on spatial scales ranging from 0.1 to 5 pc in the remnant.

#### 4. Summary and Conclusions

Chandra images and spectra support that the Puppis A supernova remnant is interacting with a complex system of interstellar clouds. In this paper, we have identified a shocked cloud behind the eastern shock front that is in a relatively late phase of evolution and is being torn apart by shear instabilities. This is the first astrophysical example of a cloud-shock interaction in this mature stage of evolution that has been identified in X-ray emission. We diagnose the evolutionary state of the interaction by direct comparison of its morphology with scaled laboratory simulations of the cloud-shock interaction. Using the X-ray morphology of the cloud, together with X-ray images and spectra, we estimate that the onset of interaction was roughly 3 cloud-crushing times, or 2000-4000 years ago, and that the initial cloud density was  $1.5\text{-}3\text{ cm}^{-3}$ . There are considerable uncertainties inherent in the details of these estimates, including the effects of electron-ion equipartition, the effect of secondary shocks on the observed temperatures, the apparent contamination of the diffuse gas by ejecta, and the relatively crude method of correspondence to the experimental results.

---

<sup>2</sup>An overlay of this [O III] image with the lower angular resolution image from the ROSAT HRI is shown in the paper by Blair et al. 1995.

The general identification of a mature cloud-shock interaction, however, is quite clear.

Closer to the forward shock in the BEK region, the shock has recently interacted with a more dense and extended obstacle. The spectral characteristics of the front portion of the BEK region are uniquely different from those in the rest of the Chandra field, with lower temperatures supported by the presence of [Fe XIV] emission, lower ionization ages, and higher column densities. These inferred spectral properties, and comparison of the X-ray/optical morphology, suggests that the remnant is now interacting with multiple clouds in this region, some of which are in the remnant foreground.

It is likely that numerous such cloud-shock interactions have left their imprint throughout the remnant. The intricate filamentary structures that pervade the X-ray images of Puppis A shown here and elsewhere resemble the final outcome of numerical hydrodynamical simulations that model the disruption of clouds as they are overrun by shocks (Stone & Norman 1992). The shocked clouds studied here will also ultimately contribute to this filamentary structure in Puppis A.

We thank Kristy Dyer and Martin Laming for stimulating discussions, and Estela Reynoso for discussion of the distance to Puppis A.

## REFERENCES

- Arendt, R. G., et al. 1990, 350, 266
- Aschenbach, B. 1994, *New Horizon of X-ray Astronomy*, ed. F. Makino & T. Ohashi, 103
- Blair, W. P., Raymond, J. C., Long, K. S., Kriss, G. A. 1995, *ApJL*, 454, L35
- Canizares, C. R., & Winkler, P. F. 1981, *ApJ*, 246, L33
- Chevalier, R. A. 2005, *ApJ*, 619, 839
- Dubner, G. M., & Arnal, E. M. 1988, *A&AS*, 75, 363
- Dubner, G. M., Braun, R., Winkler, P. F., & Goss, W. M. 1991, *AJ*, 101, 1466
- Fesen, R. A., Kwitter, K. B., Downes, R. A. 1992, *AJ*, 104, 719
- Gaensler, B. M., Bock, D. C.-J., & Stappers, B. w. 2000, *ApJL*, 537, L35
- Graham, J. R. Levenson, N. A., Hester, J. J., Raymond, J. C., & Petre, R. 1995, *ApJ*, 444, 787

- Jun, B.-I., Jones, T. W., & Norman, M. L. 1996, *ApJ*, 468, 59
- Klein, R., Budil, K. S., Perry, T. S., & Bach, D. R. 2003, *ApJ*, 583, 245
- Klein, R., McKee, C. F., & Colella, P. 1994, *ApJ*, 420, 213
- Leahy, D. A. 2003, *ApJ*, 586, 224
- Leahy, D. A. 2004, *MNRAS*, 351, 385
- Levenson, N. A., & Graham, J. R. 2005, *ApJ*, 622, 366
- Levenson, N. A., Graham, J. R., & Walters, J. L. 2002, *ApJ*, 576, 798
- Lu, F. J., & Aschenbach, B. 2000, *A&A*, 362, 1083
- Miyata, E., Tsunemi, H., Kohmura, T., Suzuki, S., & Kumagai, S. 1998, *PASJ*, 50, 2
- Patnaude, D. J., Fesen, R. A., Raymond, J. C., Levenson, N. A., Graham, J. R., & Wallace, D. J. 2002, *AJ*, 124, 2118
- Pavlov, G. G., Sanwal, D., Garmire, G. P., & Zavlin, V. E. 2002, in Slane, P. O., & Gaensler, B. M., eds., *ASP Conference Series Vol 271, Neutron Stars in Supernova Remnants*, ASP, San Francisco, 247
- Pavlov, G. G., Zavlin, V. E., & Trümper, J. 1999, *ApJ*, 511, L45
- Petre, R., Becker, C. M., & Winkler, P. F. 1996, *ApJL*, 465, L43
- Petre, R., Canizares, C. R., Kriss, G. A., & Winkler, P. F. 1982, *ApJ*, 258, 22
- Rakowski, C. E., Ghavamian, P., & Hughes, J. P. *ApJ*, 590, 846
- Reynoso, E. M., Dubner, G. G., Goss, W. M., & Arnal, E. M. 1995, *AJ*, 100, 318
- Reynoso, E. M., Green, A. J., Johnston, S., Dubner, G. M., Giacani, E. B., & Goss, W. M. 2003, *MNRAS*, 345, 671
- Ryutov, D., et al. 1999, *ApJ*, 518, 821
- Snowden, S. L., McCammon, D., Burrows, D. N., Mendenhall, J. A. 1994, *ApJ*, 424, 714
- Stone, J. M., & Norman, M. L. 1992, *ApJ*, 390, 17
- Tamura, K. 1995, Osaka University PhD Thesis

Teske, R. G., & Petre, R. 1987, ApJ, 314, 673

Winkler, P. F., & Kirshner, R. P. 1985, ApJ, 299, 981

Winkler, P. G., Tuttle, J. H., Kirshner, R. P., & Irwin, M. J. 1988, Supernova Remnants and the Interstellar Medium, Proceedings, of IAU Colloquium 101 (eds. R. S. Roger & T. L. Landecker), Cambridge: Cambridge University Press, 65

Woermann, B. Gaylard, M. J., Otrupcek, R. 2000, MNRAS, 317, 421

Table 1. Sample Spectral Fits

Region	Counts	$\chi^2, \chi^2/\nu$	$N_{\text{H}}$ ( $10^{22} \text{ cm}^{-2}$ )	kT (keV)	$n_{\text{e}t}$ ( $10^{11} \text{ cm}^{-3}\text{s}$ )	O/Ne (rel $\odot$ )
127 (bar)	8211	121.6, 1.74	0.059 (0.027-0.13)	0.57 (0.55-0.59)	7.7 (5.9-9.6)	...
139 (cap)	13700	129.0, 1.59	0.17 (0.14-0.21)	0.58 (0.56-0.60)	3.8 (3.0-4.7)	...
74 (compact)	9036	67.8, 1.17	0.33 (0.30-0.37)	0.33 (0.29-0.37)	0.49 (0.38-0.59)	...
212 (hard)	9878	106.7, 1.31	0.087 (0.050-0.12)	0.76 (0.72-0.80)	1.8 (1.4-2.2)	...
214	9790	145.3, 1.94	0.13 (0.12-0.14)	0.81 (0.78-0.84)	1.3 (1.2-1.4)	...
214	...	104.5, 1.41	0.40 (0.35-0.44)	0.66 (0.58-0.74)	0.75 (0.50-1.1)	2.6 (2.3-3.0)

\*Errors quoted are 90% confidence for one interesting parameter ( $\Delta\chi^2 = 2.7$ ).

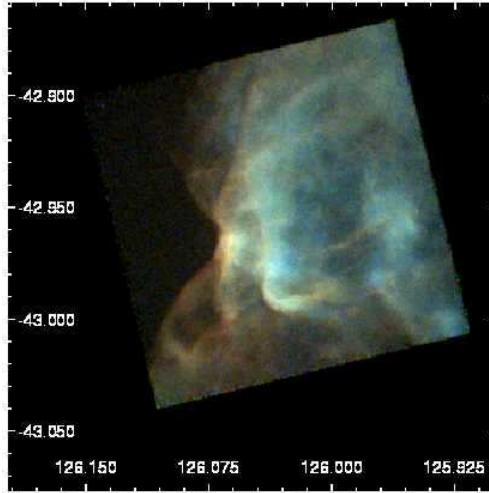


Fig. 1.— Three-color Chandra images with soft band (O) in red, medium band (Ne) in green, and hard band in blue of the BEK. The intensity scale is square-root, and J2000 coordinates are given with N pointing up.

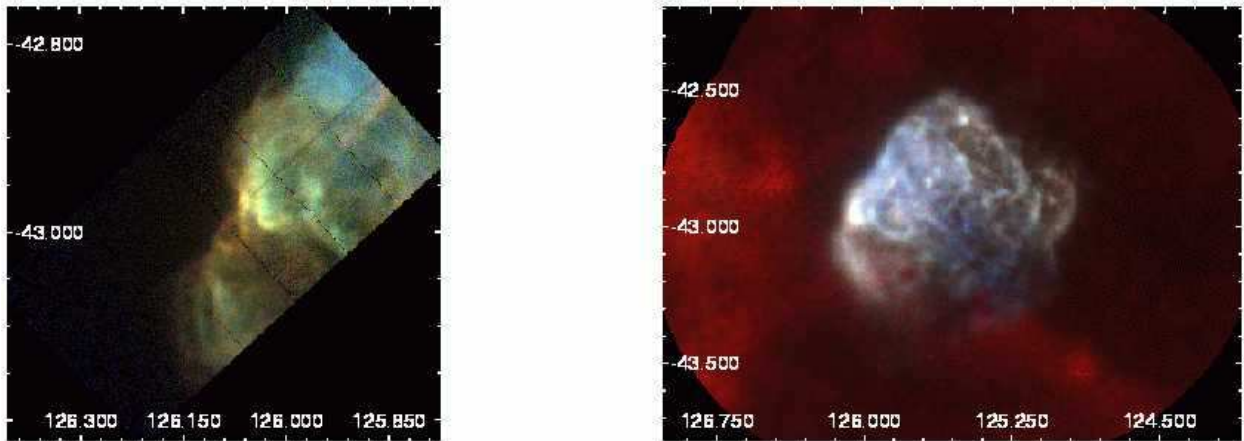


Fig. 2.— (a) Three-color image of the larger angular scale region around the BEK from the EPIC PN camera on XMM-Newton, using the same energy cuts as for the Chandra images in Figure 1. (b) Adaptively smoothed ROSAT PSPC mosaic of the entire remnant in the standard three PSPC colors: soft in red, medium in green, hard in blue (see text and Snowden et al. 1994).

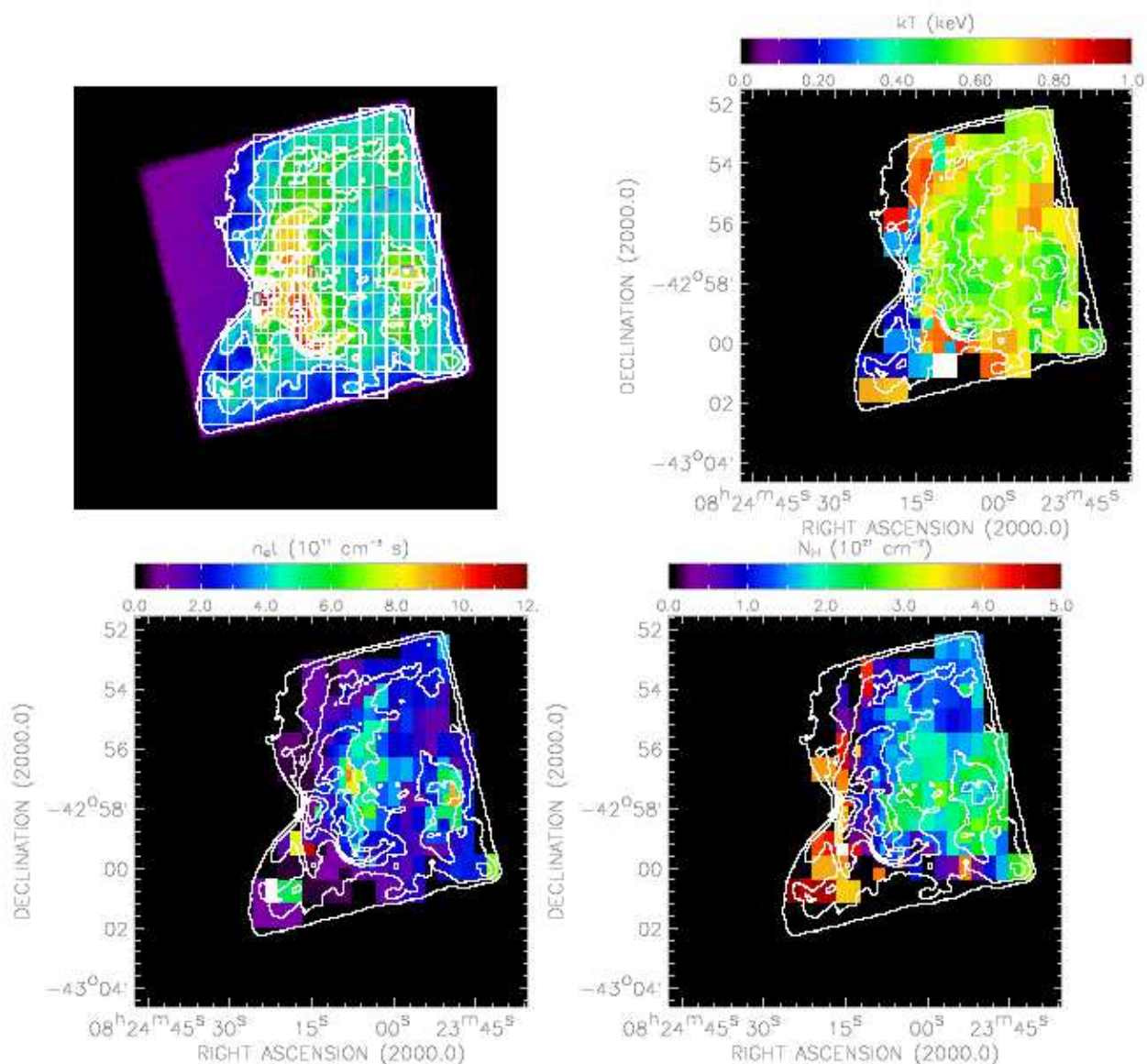


Fig. 3.— (a) BEK spectral regions overlaid on a smoothed square-root intensity image showing: a marked indentation of the X-ray emitting blast wave to the east, the compact knot just west of the indentation in red and white, the bar to the west of the compact knot running roughly north-south in red and yellow, the smaller cap in yellow and green near the western edge of the field. The spectra of the regions indicated in black are shown in Figure 4 (from left to right: compact knot, bar, hard region at top right, and cap at lower right). The same smoothed intensity contours are overlaid in each panel of this figure. (b) Temperature ( $kT$ ) map in keV; (c) Ionization age ( $n_e t$ ) map in  $10^{11} \text{ cm}^{-3} \text{ s}$ ; (d) Column density ( $N_H$ ) map in  $10^{21} \text{ cm}^{-2}$ .

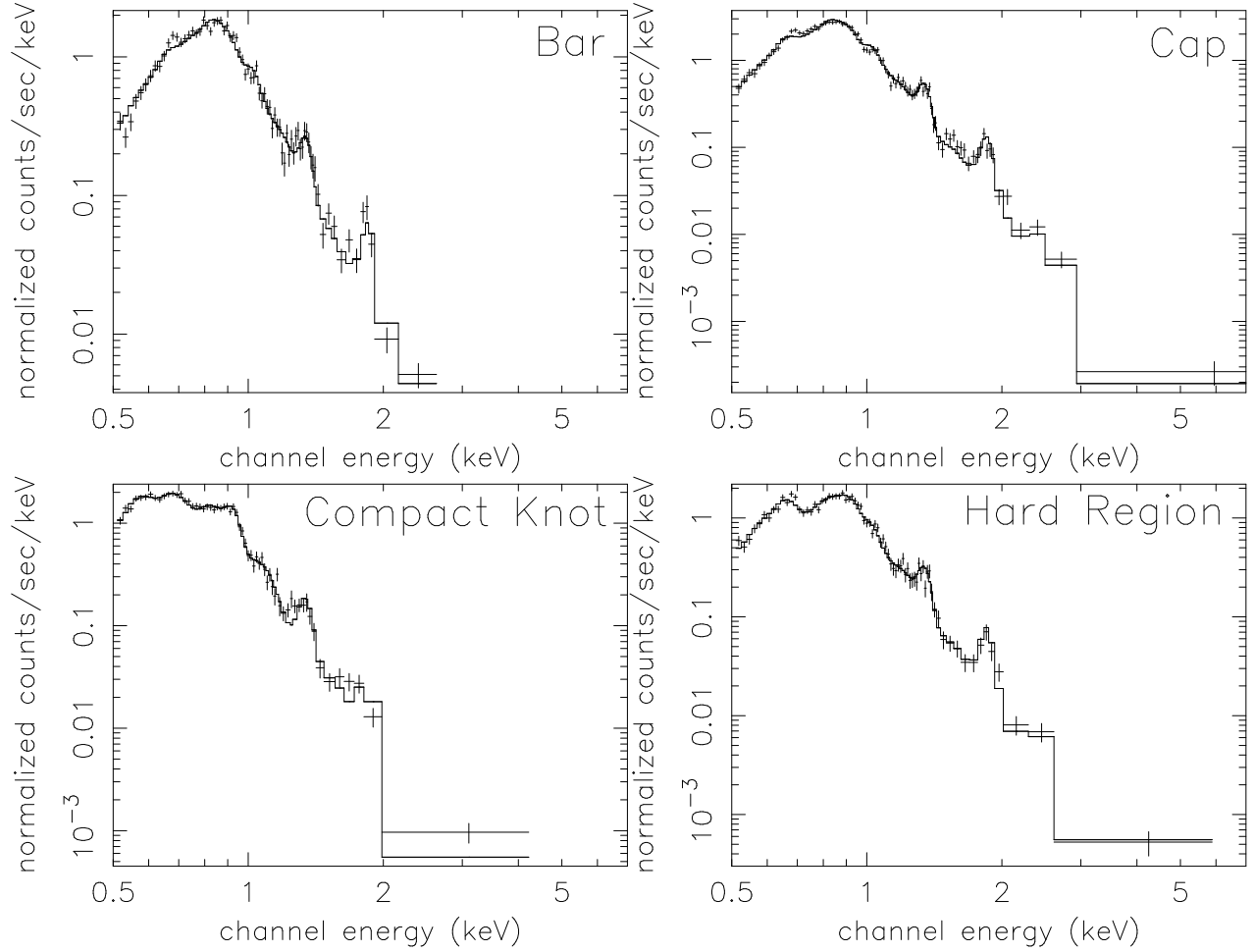


Fig. 4.— Representative spectra in the BEK field, taken from the regions indicated in Figure 3: (a) from bar and (b) cap structure; (c) from soft compact knot; (d) from a hard region north of the bar and cap. See the table for fitted parameters.

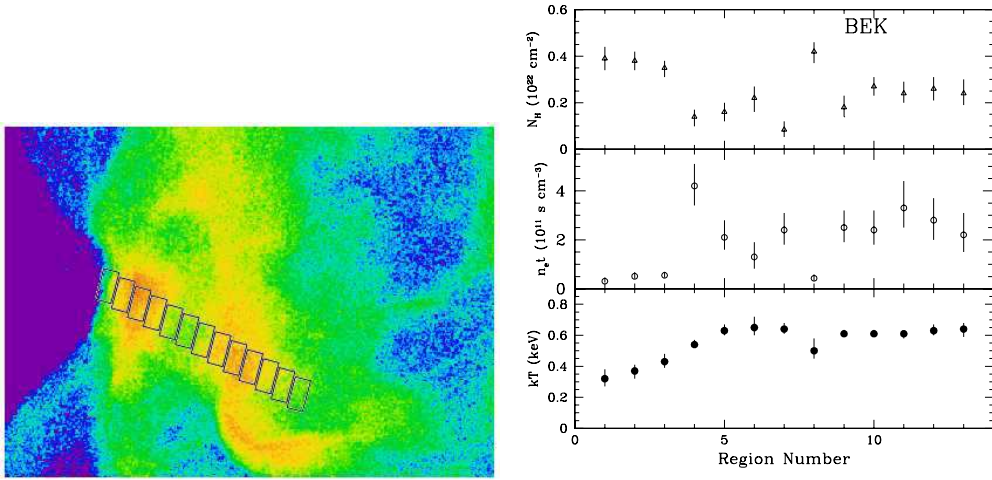


Fig. 5.— (a) Adjacent regions used to take a more detailed look at the interface between cooler  $\sim 0.3$  keV emission and the hotter  $\sim 0.6$  keV emission going from the compact knot to the bar. (b) Fitted column density, ionization age, and temperatures for these spectra. The regions are numbered successively from east to west.

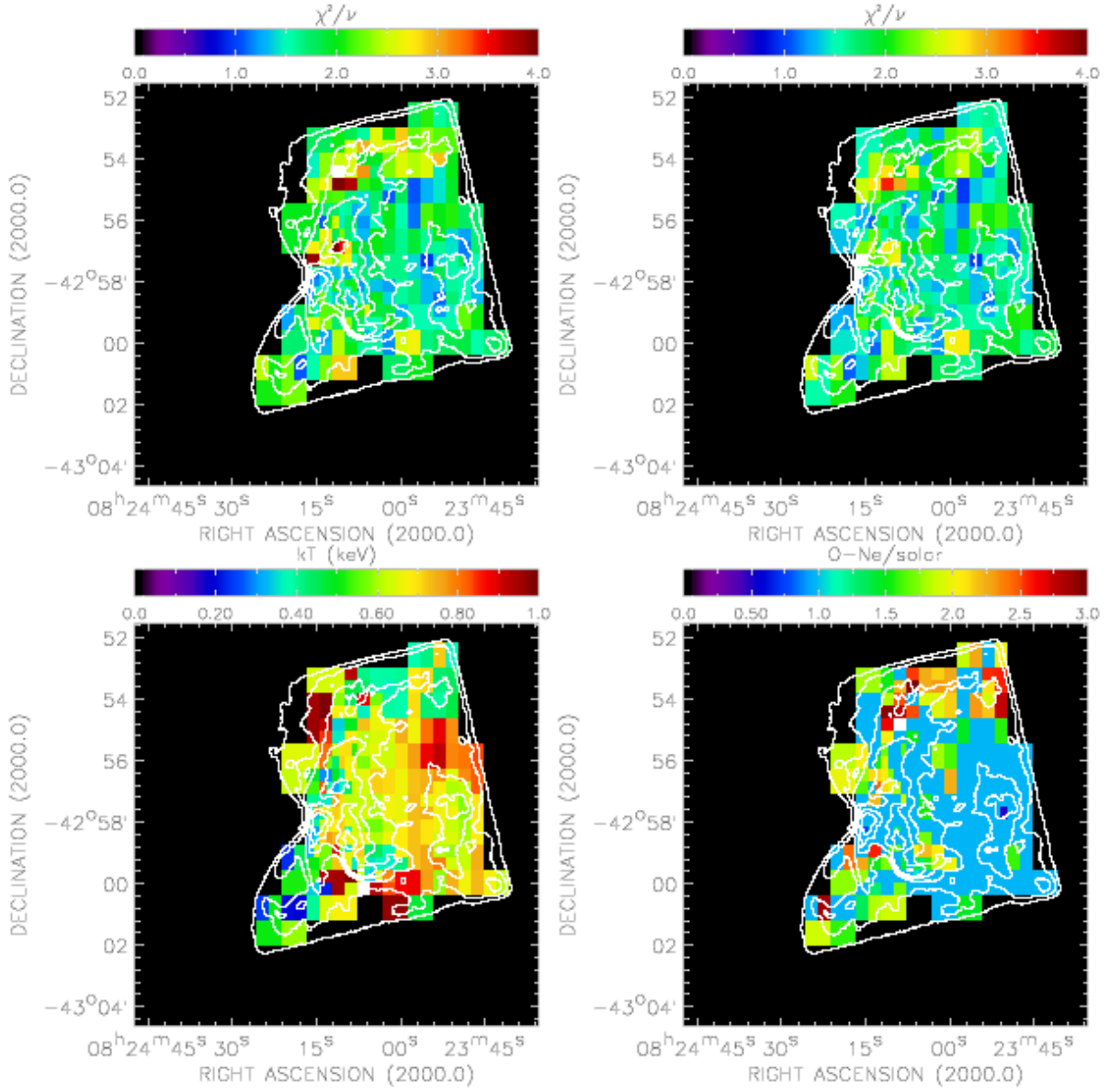


Fig. 6.— (a) Original map of  $\chi^2/\nu$ ; (b) Map of  $\chi^2/\nu$  after allowing O-Ne to be fitted; (c) Temperature (kT) map in keV when the O-Ne abundance is allowed to be freely fitted. The revised fit is accepted for the grid if the improvement in  $\chi^2$  satisfies the 0.5% probability F-test for infinite degrees of freedom ( $\Delta\chi^2/\chi_{r,new}^2 > 7.88$ ); (d) Corresponding abundance map (number abundance relative to the solar values for O and Ne in their solar abundance ratio).

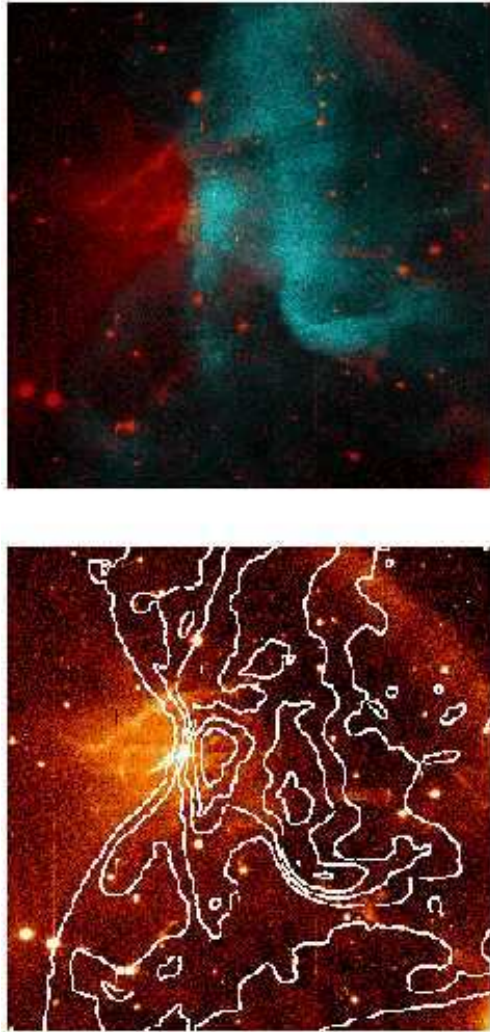


Fig. 7.— The [O III] image of Blair et al. 1995: (a) in red, with the Chandra X-ray image in blue and (b) with the Chandra X-ray contours overlaid.